



CHORUS

This is the accepted manuscript made available via CHORUS. The article has been published as:

Effect of thermal disorder on high figure of merit in PbTe

Hyounghul Kim and Massoud Kaviany

Phys. Rev. B **86**, 045213 — Published 23 July 2012

DOI: [10.1103/PhysRevB.86.045213](https://doi.org/10.1103/PhysRevB.86.045213)

Roles of Thermal Disorder in High- ZT PbTe

Hyoungchul Kim and Massoud Kaviani*

Department of Mechanical Engineering, University of Michigan, Ann Arbor, MI 48109, USA

(Dated: May 25, 2012)

With *ab initio* molecular dynamics we observe thermal disorder and find band convergence with increased temperature and close relation between thermal disorder and thermoelectric (TE) properties of *p*-doped PbTe. Lack of short-range order causes local overlap of valence orbitals and increase in density-of-states near the Fermi level. Effective mass becomes temperature dependent peaking in the converged-band regime. With classical molecular dynamics (MD) and the Green-Kubo autocorrelation decay we find reduction in lattice thermal conductivity (suppression of short- and long-range acoustic phonon transports). The described thermal-disorder roles lead to high TE figure-of-merit (ZT), and in good agreement with the experimental results.

PACS numbers: 72.20.Pa, 71.20.Nr, 63.20.Ry

I. INTRODUCTION

Thermoelectricity allows for direct conversion of heat into electrical power with significant potential for power generation. The conversion efficiency is related to TE figure-of-merit,

$$ZT = \frac{S^2 \sigma_e T}{\kappa_e + \kappa_L}, \quad (1)$$

where T , S , σ_e , κ_e , and κ_L are temperature, the Seebeck coefficient, electrical conductivity, and electronic and lattice thermal conductivities. Lead telluride (PbTe), a chalcogenide with simple rocksalt structure (space group $Fm\bar{3}m$, see Fig.1), is a well-known mid-temperature TE material for power generation¹⁻³. Its recent studies as a high- ZT material has shown (i) resonant-state enhancement of the Seebeck effect^{4,5}, (ii) reduced thermal conductivity using embedded nanostructures⁶⁻⁸, and (iii) band convergence by dopant tuning^{3,9}. In addition, there have been experimental and theoretical studies of its anharmonic lattice dynamics (ferroelectric instability)¹⁰⁻¹², however, this has not been related to its electronic band convergence and TE properties. In this letter, we examine the thermal disorder caused PbTe electronic band convergence, using first-principles calculations (including *ab initio* molecular dynamics AIMD) and investigate the roles of disorder and convergence in the charge- and phonon-related TE properties.

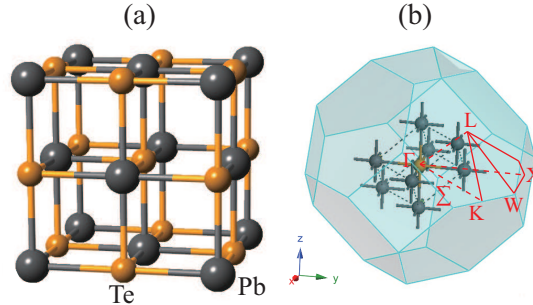


FIG. 1: (Color online) (a) Conventional cell of PbTe showing simple cubic structure. (b) The first Brillouine zone for the primitive cell of PbTe and its high symmetry k -points.

PbTe has octahedral coordination (rocksalt structure, see Fig. 1) and its lattice dynamics manifests high degree of anharmonicity^{1,10,12,13}. This reduces the phonon conductivity^{11,13}. In the thermal-disordered structure of Pb compounds, the Pb atoms are moved further off-centered compared to the chalcogen atoms, with the following trend among dislocation of compounds: $\text{PbS} < \text{PbSe} < \text{PbTe}$. Based on these, the origin of low thermal conductivity of PbTe has been explained¹¹⁻¹³. The abnormal temperature-dependent bandgap energy (i.e., increase with increase in temperature) has also been explained by lattice dynamics using the Debye-Waller factor calculations (larger Pb displacements compared to Te)¹⁴. In comparison, studies of band convergence in PbTe are very limited. Although the existence of a second valence band edge was first proposed by Allgaier¹⁵ based on the temperature dependence of the Hall effect, no exact physical explanation or direct evidence of the band convergence of PbTe has yet been reported¹⁶. However, recent studies of band convergence and its analytic model have pointed to improved TE properties in PbTe^{6,9}.

A three-band model accounts for the non-parabolicity and anisotropy of the conduction-band and the valence-band at L $\langle 111 \rangle$ points using the Kane model, while using the parabolic and isotropic behavior for the secondary valence-band along the $\Sigma \langle 110 \rangle$ direction^{9,17–20}.

II. CALCULATIONS OF TE TRANSPORT PROPERTIES

A. Thermal-disordered structures from AIMD

We investigate the high-temperature behavior of PbTe structure by obtaining the thermal-disordered structure of PbTe using AIMD with the Vienna *ab initio* simulation package²¹, i.e., we find with increase in temperature anharmonic lattice vibration distort crystal symmetry and in turn the electrons respond to the displaced ionic positions. Using the Born-Oppenheimer approximation, the atomic positions and velocities are updated with the Verlet algorithm. The forces on ions at each configuration are used to update the ionic positions at an elapsed time step and we iterate to calculate the trajectory of the system. The AIMD simulations are performed on supercells consisting 54-atoms ($3 \times 3 \times 3$ primitive cells) and 64-atoms ($2 \times 2 \times 2$ conventional cells) along with and the projector augmented wave-based density functional theory DFT (also used for the static calculations)²². Considering thermal expansion with temperature changes, we prepare the PbTe supercells with experimental results for thermally-expanded lattice parameter, $a(T) = 6.422 + (0.9546 \times 10^{-4})T + (2.615 \times 10^{-8})T^2$ for 293 to 973 K²³. The proper cell volume at each temperature is locked during AIMD calculations. The Brillouin zone (BZ) is sampled at only the gamma point. We carry out constant-temperature simulations using Nosé thermostat for 6 ps (0.2 fs time steps). After reaching equilibrium using a NVT ensemble, another calculation is performed for 11 ps (1 fs time steps), and we find good energy convergence and temperature stability. During AIMD calculations, the Fermi-Dirac smearing factor ($k_B T$, where k_B is the Boltzmann constant) for each temperature was also applied to ensure reliable thermal-disordered atomic coordinates. Finally, all temperature-dependent atomic coordinates are obtained from AIMD snapshots at each temperature.

To verify the snapshots are represent stable structures and motion, we addressed the statistical uncertainty. As noted above, two step approach is used to find a stable snapshot. As shown in Fig. 2, we find our second step simulations are fully relaxed and it provides energy-converged structures with low statistical uncertainty. Every snapshot is average of 64 displaced coordinates of PbTe and is used in the calculations of the transport properties. (The error bars of the atomic displacement of each atom will be shown in Fig. 4, indicate the statistical uncertainty.) These verification processes are used to ensure shots are indeed representative.

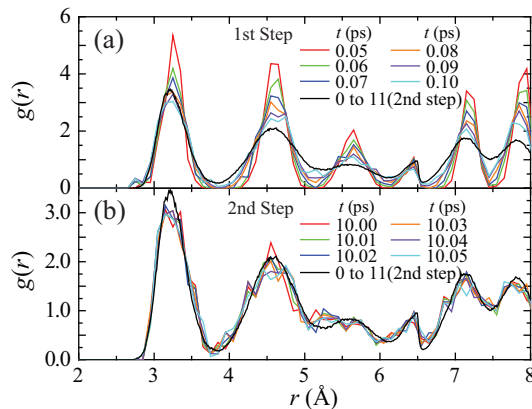


FIG. 2: (Color online) Time-dependent evolution of radial distribution functions $g(r)$ of PbTe supercell at $T = 700$ K. Each snapshot is average of 64 displaced coordinates obtained from (a) initial, and (b) a well-converged AIMD step. Average $g(r)$ of all snapshots (2nd step, 0 to 11 ps) are also shown.

B. Electronic structures and transport properties

Our electronic calculations employs the full-potential linearized augmented plane-wave method²⁴ as implemented in the WIEN2k code²⁵. We calculate all TE transport properties of thermal-disordered p -type PbTe using WIEN2k and

BoltzTraP²⁶ codes, and a MD code written for this problem. All PbTe transport properties are calculated from the common DFT band energies (0 K). However, those DFT band energies obtained from thermally-disordered structure (AIMD snapshots at each temperature) and the Fermi-Dirac smearing factors were also used in the transport-property calculations. We expect/show these two temperature effects (atomic configurations and smearing) are sufficient to illustrate the abnormal changes of PbTe properties with temperature. The muffin-tin radii are chosen to be 2.5 a.u. for all atoms. The plane-wave cutoff $Rk_{\max} = 7.0$ suffices for good convergence. Due to the large atomic masses (Pb and Te), spin-orbit interaction is included for the relativistic effects. Convergence of the self-consistent calculation cycle is performed using 2769 (for frozen structure) and 36 (for high-temperature structure) k -points inside the reduced BZ to within 0.0001 Ry with a cut-off of -6.0 Ry between the valence and the core states. Since TE transport properties are sensitive to band structures near the Fermi surface, we use the Engel-Vosko generalized gradient approximation to avoid the underestimation of bandgap energy (a well-known problem with DFT calculations)²⁷. The spin-orbit interaction is also included for the relativistic effects. In the transport calculations, the original k -mesh is interpolated onto a mesh five times as dense and the eigenenergies are found with BoltzTraP code. Within the Boltzmann transport theory the temperature- and doping-level-dependent conductivity $\sigma_e(T, \mu_e)$ and the Seebeck coefficient $S(T, \mu_e)$ are given by

$$\sigma_{e,\alpha\beta}(T, \mu_e) = \frac{1}{V} \int \sigma_{e,\alpha\beta}(E_e) \left[-\frac{\partial f_e^\circ(T, E_e)}{\partial E_e} \right] dE_e, \quad (2)$$

$$S_{\alpha\beta} = \sum_{\gamma} (\sigma_e^{-1})_{\alpha\gamma} \nu_{e,\beta\gamma}, \quad (3)$$

with

$$\nu_{e,\alpha\beta}(T, \mu_e) = \frac{1}{eTV} \int \sigma_{e,\alpha\beta}(E_e) (E_e - \mu_e) \left[-\frac{\partial f_e^\circ(T, E_e)}{\partial E_e} \right] dE_e, \quad (4)$$

where E_e is band energy, f_e° is the Fermi-Dirac equilibrium distribution, μ_e is the chemical potential, and V is the volume. The energy projected conductivity tensor is

$$\sigma_{e,\alpha\beta}(E_e) = \frac{1}{N} \sum_{i,\mathbf{k}} e^2 \tau_{e,i,\mathbf{k}} v_{e,\alpha}(i, \mathbf{k}) v_{e,\beta}(i, \mathbf{k}) \frac{\delta(E_e - E_{e,i,\mathbf{k}})}{dE_e}, \quad (5)$$

where i is the band index, \mathbf{k} is the wave vector, N is a normalization depending on the number of k -points sampled in the BZ, $\tau_{i,\mathbf{k}}$ is a relaxation time, and $v_{e,\alpha}(i, \mathbf{k})$ is the i component of band velocity $\nabla_{\mathbf{k}} E_e(\mathbf{k})$.

C. Classical MD and lattice conductivity calculations

Previous lattice thermal conductivity results of PbTe using classical MD^{28,29} are limited and require special attention due to the strong anharmonic coupling effects¹¹. Using atomic substitutions²⁸ and various vacancy configurations²⁹, reduced lattice thermal conductivity of PbTe has been predicted using classical MD. In order to consider the anharmonic behaviors of PbTe structures, we use the thermal-disordered configurations (from AIMD) and the potential models appropriate for the covalent and rigid-ionic bonds. For these bonds, we use the Morse and the three-cosine interatomic potentials with effective ionic charges¹², parameterized for two-body (Pb-Te and Te-Te) and three-body (Te-Pb-Te) interactions, i.e.,

$$\varphi(r_{ij}) = \varphi_o \{ [1 - \exp(-a(r_{ij} - r_o))]^2 - 1 \}, \quad (6)$$

$$\varphi(\theta_{ijk}) = (1/2) \varphi_\theta (\cos \theta_{ijk} - \cos \theta_o)^2, \quad (7)$$

where φ_o , r_{ij} , and θ are the dissociation energy, interatomic separation distance, and bond angle. The parameters φ_o , r_{ij} , and θ are determined by fitting to both the *ab-initio* calculated total energy and the experimental elastic constants. Utilizing a multi-variable fitting procedure in GULP (general utility lattice program)³⁰, we obtain the parameters listed in Table I. The fitted pair potential undergo GULP optimization of the crystal structure under constant pressure. All related thermo-mechanical properties (e.g., elastic constants, bulk modulus, shear modulus, the Grüneisen parameter, and thermal expansion coefficient) are listed in Table II and compared with the reported experiments with good agreements.

TABLE I: The Morse and the three cosine interatomic potential parameters for PbTe. The effective atomic charges of Pb and Te are 0.72 and -0.72¹², respectively.

Two-body	φ_o (eV)	a (1/Å)	r_o (Å)	Three-body	φ_θ (eV)	θ_o (°)
Pb-Te	0.465	0.863	3.68	Te-Pb-Te	0.680	90.0
Te-Te	0.394	1.51	4.22			

TABLE II: Comparison of bulk mechanical properties found from the interatomic potentials with those from experiments. C_{ij} , B , G , γ_G , and α are elastic constants, bulk modulus, shear modulus, Grüneisen parameter, and thermal expansion coefficient.

	C_{11} (GPa)	C_{12} (GPa)	C_{44} (GPa)	B (GPa)	G (GPa)	γ_G	α (10^{-5} /K)
Reference ³¹	128.1	4.4	15.1	-	-	-	-
Reference ³²	105.3	7.0	13.2	39.8	21.4	-	-
Reference ³³	108.0	7.7	13.4	41.1	-	-	-
Reference ³⁴	-	-	-	-	-	1.45	-
Reference ³⁵	-	-	-	-	-	-	1.8
This work	108.0	7.5	15.1	41.0	21.0	1.66	1.78

The lattice thermal conductivity tensor κ_L is determined using the equilibrium MD results and the Green-Kubo heat current autocorrelation function (HCACF) decay³⁶⁻³⁸, i.e.,

$$\kappa_L = \frac{1}{k_B T^2 V} \int_0^\infty \langle \mathbf{q}(t) \mathbf{q}(0) \rangle dt, \quad (8)$$

where t is time, and $\langle \mathbf{q}(t) \mathbf{q}(0) \rangle$ is the HCACF tensor. \mathbf{q} is

$$\mathbf{q} = \frac{d}{dt} \sum_i E_i \mathbf{r}_i = \sum_i E_i \mathbf{u}_i + \frac{1}{2} \sum_{i,j} (\mathbf{F}_{ij} \cdot \mathbf{u}_i) \mathbf{r}_{ij}, \quad (9)$$

where E_i , \mathbf{r}_i , and \mathbf{u}_i are the energy, position, and velocity vectors of particle i , and \mathbf{r}_{ij} , and \mathbf{F}_{ij} are the interparticle separation and force vectors between particle i and j . After checking the size effect of MD, average are found over all three directions for a system consisting of $8 \times 8 \times 8$ conventional unit cells (4096 atoms). The Verlet leapfrog algorithm with the Nosé-Hoover thermostat and the Berendsen barostat are used in NpT ensemble for 200 ps and then in NVE for 100 ps to reach the equilibrium. Then 3000 ps raw data are obtained for the calculation of \mathbf{q} . The resultant HCACFs were then directly integrated and the κ_L was set as the average value in the stable regime of the integral.

D. Analytic models for TE properties

The TE properties are obtained using the Onsager TE coupling and the Boltzmann transport equation with energy-dependent relaxation time $\tau_e(E_e)$ ^{3,7,17,20,39-41}. The differential electrical conductivity $\sigma_{d,e,\alpha}(E_e)$ is^{42,43}

$$\sigma_{d,e,\alpha}(E_e) = e^2 \tau_e(E_e) v_{e,\alpha}^2(E_e) D_{e,\alpha}(E_e) \left(-\frac{\partial f_e^0}{\partial E_e} \right), \quad (10)$$

where τ_e is the relaxation time, $v_{e,\alpha}$ is the group velocity, and $D_{e,\alpha}$ is the electronic density-of-states. Here $v_{e,\alpha}$ is given by

$$v_{e,\alpha} = \left\{ \frac{2}{m_{i,e,\alpha}} \gamma_\alpha(E_e) \left[\frac{d\gamma_\alpha(E_e)}{dE_e} \right]^{-2} \right\}^{1/2}, \quad (11)$$

and $D_{e,\alpha}(E_e)$ is given by

$$D_{e,\alpha}(E_e) = \frac{2^{1/2} m_{i,e,\alpha}^{3/2}}{\pi^2 \hbar^3} \gamma_\alpha(E_e)^{1/2} \left[\frac{d\gamma_\alpha(E_e)}{dE_e} \right], \quad (12)$$

where \hbar is the reduced Planck constant, $m_{i,e,\alpha}(T)$ is the temperature-dependent density-of-states effective mass at α point, $\gamma_L(E_e) = E_e(1 + E_e/\Delta E_{e,g,L})$ for the non-parabolic bands (i.e., conduction and L-point light-hole valence),

while $\gamma_\Sigma(E_e) = E_e$ for the parabolic Σ -point heavy-hole valence band^{19,20,39–41}. Here $\Delta E_{e,g,\alpha}$ is the bandgap energy at α point. The carrier mobility depends on $\tau_e(E_e)$ and effective mass $m_{i,e,\alpha}$ which are also temperature dependent. The $\tau_e(E_e)$ is phonon dominated (three mechanisms). The AIMD calculated $m_{i,e,\alpha}(T)$ for all bands are used in Eqs. (11) and (12). The carrier concentration n_i is

$$n_i = \int_{E_{\text{CBM}}}^{\infty} D_{e,\text{C}}(E_e) f_e^\circ(E_e) dE_e - \left\{ \int_{-\infty}^{E_{\text{VBM,L}}} D_{e,\text{L}}(E_e) [1 - f_e^\circ(E_e)] dE_e + \int_{-\infty}^{E_{\text{VBM},\Sigma}} D_{e,\Sigma}(E_e) [1 - f_e^\circ(E_e)] dE_e \right\}. \quad (13)$$

The electrical conductivity σ_e is

$$\sigma_{e,\alpha} = \int_0^\infty \sigma_{d,e,\alpha}(E_e) dE_e \quad \text{and} \quad \sigma_e = \sum_\alpha \sigma_{e,\alpha}. \quad (14)$$

The Seebeck coefficient S is

$$S_\alpha = \frac{1}{eT} \left[\frac{\int_0^\infty \sigma_{d,e,\alpha}(E_e) (E_e - E_F) dE_e}{\int_0^\infty \sigma_{d,e,\alpha}(E_e) dE_e} \right] \quad \text{and} \quad S = \frac{\sum_\alpha S_\alpha \sigma_\alpha}{\sum_\alpha \sigma_\alpha}. \quad (15)$$

The electronic thermal conductivity κ_e is

$$\kappa_{e,\alpha} = \frac{1}{e^2 T} \left\{ \int_0^\infty \sigma_{d,e,\alpha}(E_e) (E_e - E_F)^2 dE_e - \frac{[\int_0^\infty \sigma_{d,e,\alpha}(E_e) (E_e - E_F) dE_e]^2}{\int_0^\infty \sigma_{d,e,\alpha}(E_e) dE_e} \right\} \quad \text{and} \quad \kappa_e = \sum_\alpha \kappa_{e,\alpha}. \quad (16)$$

Including the lattice thermal conductivity from MD, then ZT is obtained from Eq. (1).

III. RESULTS AND DISCUSSION

A. Lattice dynamics of thermal-disordered structures

Using AIMD and classical MD calculations, we verified the abnormal anharmonic lattice dynamics of PbTe over the temperature range. The lattice coordinates of each atom for each time step is collected, and the results are averaged to obtain overall radial distribution function $g(r)$, as shown in Fig. 3. Our simulations successfully reproduce all related lattice dynamics results^{10,12}, peak broadening with rising temperature and non-Gaussian asymmetry.

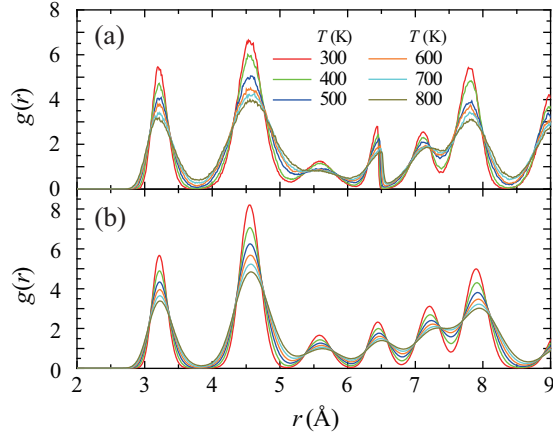


FIG. 3: (Color online) Calculated radial distribution functions of PbTe supercell obtained from (a) AIMD, and (b) classical MD.

Figure 4 shows the RMS atomic off-centering (compared to 0 K) of the ions as a function of temperature. Under the Debye harmonic approximation for isotropic lattice, the RMS displacement $\bar{\Delta}$ is³⁶

$$\bar{\Delta} \equiv \langle [(\mathbf{d}_j - \mathbf{d}_o) \cdot \mathbf{s}_j]^2 \rangle^{1/2} = \left\{ \frac{3\hbar}{m\omega_D} \left[\frac{1}{4} + \left(\frac{T}{T_D} \right)^2 \int_0^{T_D/T} \frac{x dx}{e^x - 1} \right] \right\}^{1/2}, \quad (17)$$

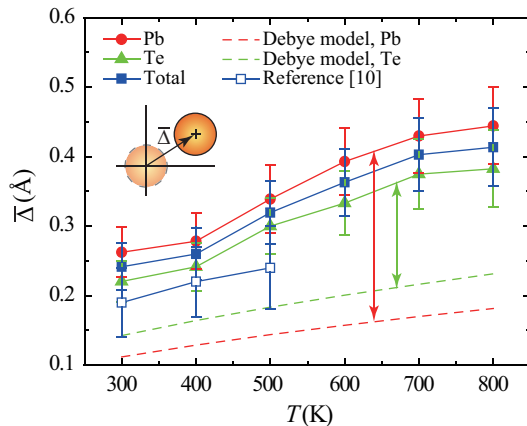


FIG. 4: (Color online) Variation of the RMS atomic local off-centering in PbTe, as a function of temperature. The Debye harmonic model prediction is also shown, with markers for differences with AIMD results. The inset image marks this RMS displacement.

where \mathbf{d}_j and \mathbf{d}_o are the displacement vectors of the atom j and the central atom, \mathbf{s}_j is the equilibrium position unit vector of the atom j , T_D is the Debye temperature, and ω_D is the Debye frequency ($= k_B T_D / \hbar$). The Debye model is more realistic model than the Einstein model, all atoms vibrate as harmonic oscillator with one frequency (ω). The Debye model also assumes the atoms vibrate as harmonic oscillators, but now with a distribution of frequencies which is proportional to ω^2 and extends to the Debye frequency ω_D . So, we can compare the difference between the Debye model and our AIMD predictions in terms of the anharmonicity. The results for this relation are also shown in Fig. 4 and the contrast (shown with vertical arrows) demonstrates the anharmonic effect predicted by AIMD. Among the symmetry-equivalent displaced sites, the amplitude of the Pb displacement is larger than that of Te atoms. This result is highly consistent with the Debye-Waller factor calculation¹⁴, i.e., abnormal bandgap energy increase with temperature. In addition to that, two well-known physical properties related to solid anharmonicity, the Grüneisen parameter and thermal expansion coefficient, are also listed in Table II. The calculated results are in good agreement with the reported values in the literatures^{34,35} and show the extent of anharmonicity. The vibration-mode frequencies of Pb and Te are noticeably different, i.e., the Te ions constitute the optical frequency peak ($f_{o,Te} \sim 2.3$ THz), while the Pb ions dominate in the acoustic regime ($f_{o,Pb} \sim 1.5$ THz). These features cannot be explained with the harmonic or quasi-harmonic models for the lattice dynamics.

B. Temperature-dependent electronic structures

From the orbital model perspective, the thermal disorder causes local orbital overlapping. Figures 5(a) to (c) show the equilibrium atomic positions at 0, 300, and 700 K along with their charge density distribution. In the presence of thermal disorder, the orbital overlaps increase significantly with temperature. At high temperature, local charge densities are distorted and the valence band distributions are altered. Also, the distorted D_e (total and partial)

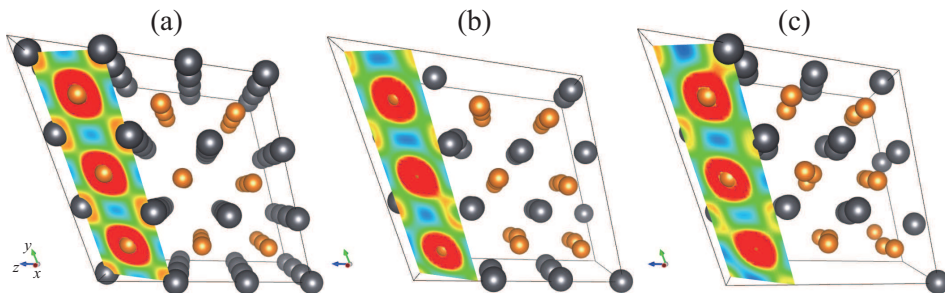


FIG. 5: (Color online) The charge densities and atomic positions of PbTe, for (a) $T = 0$, (b) 300, and (c) 700 K. A slice (101) illustrates the electron-density distribution (a distance from origin of 16.8 \AA). The charge density contours are for 0 (blue) to 0.289 (red) $e\text{\AA}^{-3}$.

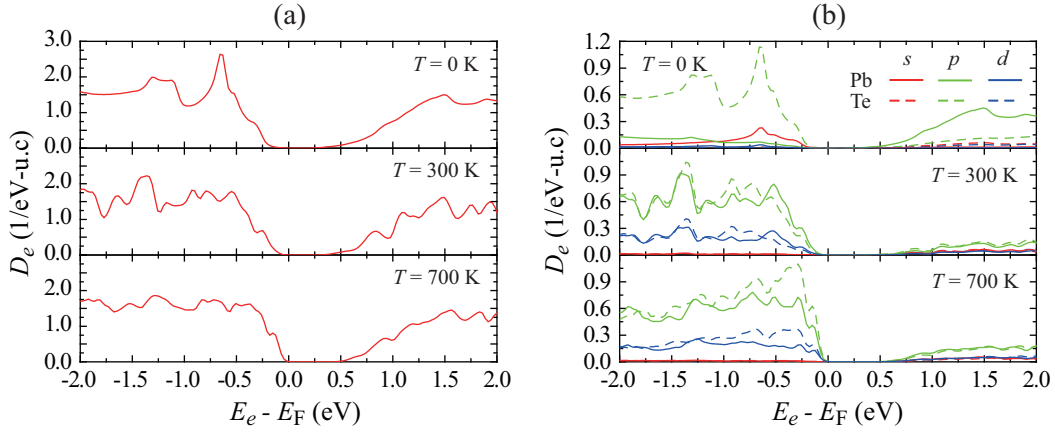


FIG. 6: (Color online) (a) Electronic density-of-states for PbTe using static DFT (0 K) and AIMD calculations (300 and 700 K). (b) Projected electronic density-of-states for PbTe, showing the s , p , and d orbital contributions. Frozen ($T = 0$ K), and thermal-disordered structure at 300 and 700 K are shown.

plots are shown in Fig. 6. At high temperatures the vibration amplitudes are substantial and modify the screening properties of the electron density⁴⁴. The D_e for the structures at 300 and 700 K are compared with the frozen structure in Fig. 6(a). The static $D_e(T = 0$ K) is not populated at the top of the valence bands, indicating the light hole at L-point, a non-parabolic Kane distribution at the valence edge. The onset of appearance of much larger hole effective mass starting at ~ -0.2 eV below the edge, is manifestation of a resonance near -0.25 eV. It results from the heavy hole in the Σ -direction¹⁶. At 0 K, this strongly increases $D_e(T)$ below -0.2 eV and is the reason for the unusual doping and temperature dependence of the TE power factor¹⁶. Compared to $D_e(T = 0$ K), the thermal disorder of PbTe structure makes for unique modifications in the $D_e(T)$, as shown in Fig. 6(a). The AIMD results for $D_e(T)$ show the band convergence of the heavy and light holes at high temperatures. First, there is a transition from the non-parabolic (low T) to parabolic (high T) $D_e(T)$ in a principal valence band. Second, comparing 0 and 700 K, the sharp $D_e(T)$ peak (near -0.2 eV, 0 K) splits into two peaks (near -0.12 and -0.4 eV, 700 K). These are highly related with the band convergence at high temperatures. The projected D_e plots [Fig. 6(b)] for $T = 0, 300$ and 700 K indicate the orbital contributions to valence band change with temperature. Also they demonstrate that the local orbital overlaps and the valence band distortion become significant with increased temperature. For $T = 0$ K, the Te $5p$ orbital dominate contribution to the first and second valence band of PbTe. Contributions from Pb ($6p$ and $5d$) and Te ($4d$ and $5p$) to the formation of valence band are found at higher temperatures, while contribution from Te $5p$ slightly diminishes. As a result, the thermal disorder and the corresponding increase in the local orbital overlaps (i.e., contributions from Pb $5d$, Pb $6p$, and Te $4d$ orbitals at 700 K) alter the distribution of the valence bands of PbTe at high temperatures.

Thermal-disorder bond anharmonicity leads to the phonon-phonon Umklapp and normal scatterings and reduction of phonon conductivity at high temperatures^{11,13,44}. In such rocksalt group IV-VI semiconductors, the outer s electrons and part of the p electrons are non-bonding and are expected to form a shell of relatively large radius¹³. This is the well-known reason for the high anharmonicity of the bonds in these materials and the ultimate cause of their low lattice thermal conductivity^{11,13,44}. Further results on thermal-disorder lattice thermal conductivity (using classical MD) will be given in later paragraphs. The calculation of the band structures (Fig. 7) and bandgap energies (Fig. 8) as a function of temperature are important in explaining the band convergence. The calculated band structures of PbTe supercell provide a clear evidence for band convergence at high temperature (above 450 K), the secondary valence band in the Σ -direction is overcome by the first valence band of L-point and PbTe becomes an indirect bandgap. From the band structures and the electronic density-of-states, we have also verified the bandgap energy changes with temperature (Fig. 8). The temperature dependence of the bandgap energy $\Delta E_{e,g}$ for PbTe is modeled⁴¹ as $\Delta E_{e,g} = 0.19 + (0.42 \times 10^{-3})T$ for $T \leq 400$ K and $\Delta E_{e,g} = 0.358$ eV for $T > 400$ K, in good agreement with experimental results⁴⁵. Noting that the general underestimation of the bandgap energy in DFT calculation, the calculated results have a similar behavior as the experiment.

Such thermal disorder electronic band alterations are quantified by temperature-dependent $m_{i,e,\alpha}(T)$. Some previous analyses treated this as constant value $m_{i,e,\alpha}^0$, or semi-temperature dependent $m_{i,e,\alpha}(T) = m_{i,e,\alpha}(0)[\Delta E_{e,g,\alpha}(T)/\Delta E_{e,g,\alpha}(0)]^{1,5,7,9,19,20}$. Using the DFT band structure of the thermal-disordered PbTe, we calculate the effective masses for each band in at BZ points and direction (fitted to parabolic model) as a function of temperature. The band effective mass $(m_{i,e,\alpha})_b$ is $1/(m_{i,e,\alpha})_b = (1/\hbar^2)[\partial^2 E_e(\mathbf{k})/\partial \mathbf{k}^2]_\alpha$ ($i = h$ or e and α is location

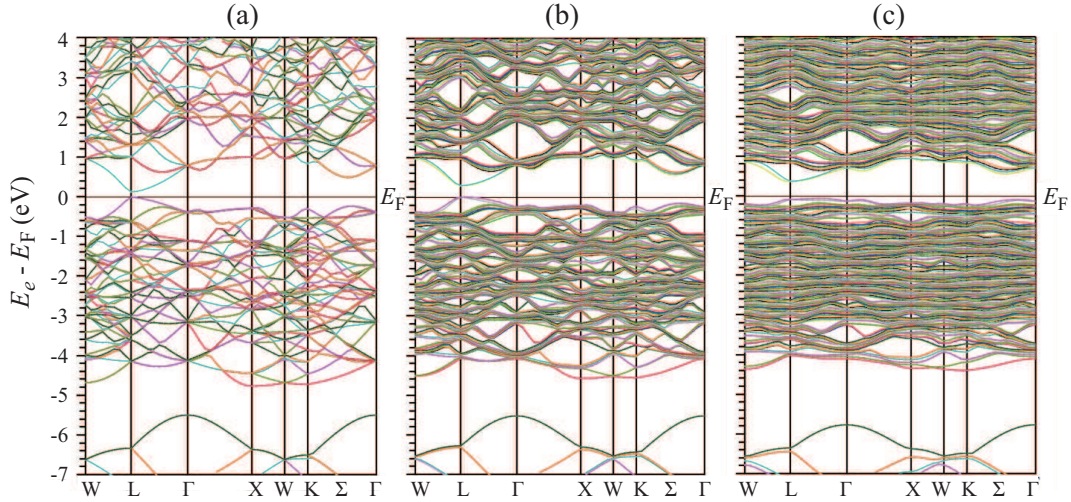


FIG. 7: (Color online) Calculated band structures of PbTe supercell ($3 \times 3 \times 3$ primitive cell) at (a) $T = 0$ K, (b) 300 K, and 700 K.

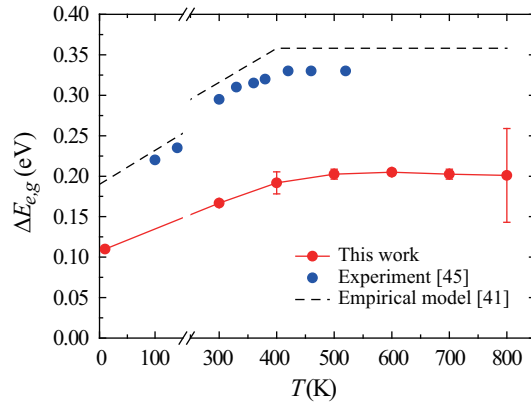


FIG. 8: (Color online) Variations of PbTe bandgap energy as a function of temperature. The experimental results and the proposed empirical model results are also shown.

in BZ)^{9,36}. This can be written in the tensor form as

$$M_{ij}^{-1} = \frac{1}{\hbar^2} \frac{\partial^2 E_e(\mathbf{k})}{\partial k_i \partial k_j} \text{ and } m_{e,e} = [\det |M_{ij}|]^{1/3}. \quad (18)$$

With the assumed parabolic E_e - k relationship at band extrema, the parabolic E_e can be generalized to

$$E_e = E_{e,o} + A_x(k_x - k_{o,x})^2 + A_y(k_y - k_{o,y})^2 + A_z(k_z - k_{o,z})^2, \quad (19)$$

TABLE III: The calculated longitudinal and transverse components of the effective electron (or hole) masses at the L- and Σ -points, as a function of temperature.

T (K)	Longitudinal			Transverse		
	$ m_{e,e,L,l}/m_e $	$ m_{h,e,L,l}/m_e $	$ m_{h,e,\Sigma,l}/m_e $	$ m_{e,e,L,t}/m_e $	$ m_{h,e,L,t}/m_e $	$ m_{h,e,\Sigma,t}/m_e $
300	0.141	0.167	1.66	0.0438	0.0563	0.243
400	0.102	0.161	1.75	0.0459	0.0704	0.168
500	0.208	0.134	2.50	0.0420	0.0592	0.198
600	0.204	0.186	2.12	0.0521	0.0876	0.162
700	0.196	0.231	1.25	0.0495	0.113	0.198
800	0.185	0.441	0.96	0.0651	0.122	0.219

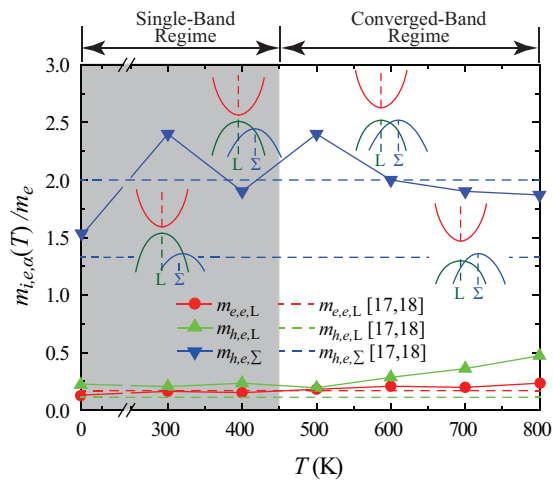


FIG. 9: (Color online) Temperature dependent the density-of-states effective masses $m_{i,e,\alpha}(T)$ obtained from DFT-AIMD. Two regimes, single- and converged-band, are also defined. The band-alignment evolution with temperature, is also illustrated. m_e is electron mass.

where coefficient A_i is constant and $(k_{o,x}, k_{o,y}, k_{o,z})$ is the coordinate of band minima/maxima. Assuming isotropic dispersion at specific point, the effective mass tensor has equal diagonal tensor elements $m_{e,e,xx} = m_{e,e,yy} = m_{e,e,zz}$ (off-diagonal elements are zero $m_{e,e,ij}^{-1} = 2A_i\delta_{ij}$) and all A_i 's are equal. Thus the effective mass tensor reduces to $m_{e,e} = 1/2A_i$. In order to maintain such scalar calculation, each components, longitudinal and transverse, of effective mass is calculated independently. The electron/hole pockets of PbTe can be characterized by a longitudinal mass ($m_{i,e,l}$) along the corresponding direction and two transverse masses ($m_{i,e,t}$) in the plane perpendicular to the longitudinal direction (with above parabolic-isotropic assumption). The value for each direction is quite different (i.e., longitudinal components are always larger than transverse) and this holds for the temperature range. This is in good agreement with a well-known feature of PbTe. The calculated effective mass components are shown in Table III. The density-of-states effective mass $m_{i,e,\alpha} = N_{i,\alpha}^{2/3}(m_{i,e,\alpha})_b = N_{i,\alpha}^{2/3}(m_{i,e,\alpha,l}m_{i,e,\alpha,t}^2)_b^{1/3}$, where $N_{i,\alpha}$ is orbital degeneracy of each valley ($N_{e,L} = N_{h,L} = 4$ and $N_{h,\Sigma} = 12^{1,9,19}$). The results for the electron and hole $m_{i,e,\alpha}$, as a function of temperature, are shown in Fig. 9. Note that the electron/hole effective mass at $T = 0$ K and band locations L- and Σ -points are $m_{e,e,L} = 0.130m_e$, $m_{h,e,L} = 0.225m_e$, and $m_{h,e,\Sigma} = 1.51m_e$. These are very close to those reported in¹⁸. Below 450 K, labeled as the "single-band regime", the L-point dominates and it is a light hole band. For $450 < T < 800$ K, labeled as the "converged-band regime", the heavy hole of Σ -point band become curved (be lighter) and matches with the light hole L-point band. Simultaneously, the promotion of the holes from the light to heavy valence bands increases $m_{h,e,\Sigma}$ in the converged regime. Thus the two bands converge and play a central role as the combined first valence band (light and heavy hole). So, the resultant effective mass increases and peaks around 500 K. These clearly show the band convergence effect in $450 < T < 800$ K.

C. TE transport properties with thermal-disordered structures

As described in method section, the transport calculations are done using the Boltzmann transport equations with energy-dependent relaxation time $\tau_e(E_e)$. Although $\tau_e(E_e)$ can be determined from the wave function and the perturbation potential obtained from the first-principle calculations, this is very challenging. Here instead we use the relaxation time models^{7,13,20,39,40,46} with three dominant electron scattering mechanisms^{40,46}, namely, i) acoustic (A), ii) optical with deformation potential couplings (DO), and iii) optical phonons with polar coupling (OP). The total $\tau_e(E_e)$, using the Matthiessen rule, is

$$\frac{1}{\tau_e(E_e)} = \sum_{i=1-3} \frac{1}{\tau_{e-p,i}(E_e)}, i = A, OD, \text{ or } OP. \quad (20)$$

The models and their parameters are given in^{7,13,20,39,40,46}. Figure 10 shows the calculated energy-dependent relaxation times as a function of electron energy, for $T = 300$ and 700 K. At low E_e (practical doping), the electron-optical phonons scattering with polar coupling is dominant.

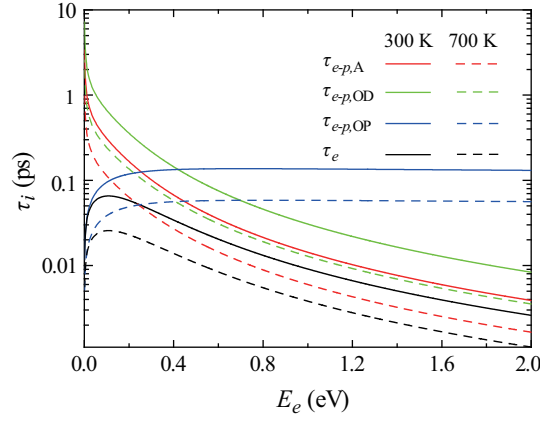


FIG. 10: (Color online) Calculated energy-dependent electron-phonon relaxation times, for 300 and 700 K. The subscripts A, OD, and OP refer to acoustic, optical with deformation potential couplings, and optical with polar coupling.

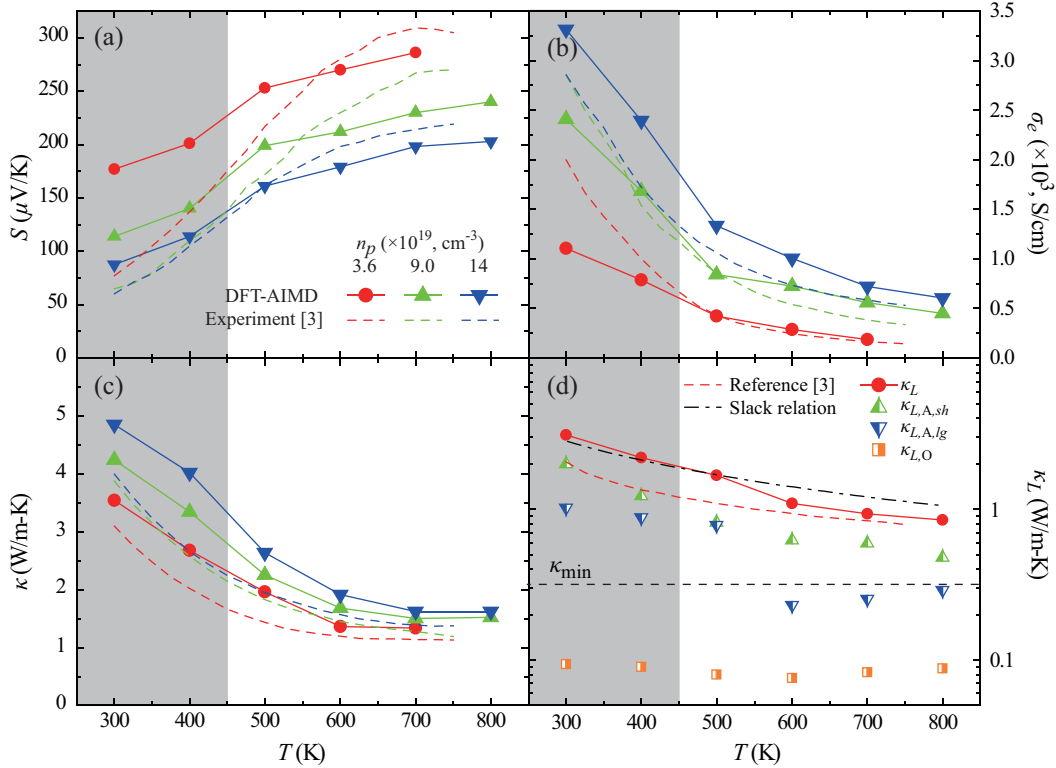


FIG. 11: (Color online) Predicted TE properties of PbTe, and comparison with experiments³. (a) Temperature dependence of the Seebeck coefficient, (b) electrical conductivity, and (c) total thermal conductivity, for three different carrier concentrations n_p . (d) Temperature variations of lattice thermal conductivity and its short- and long-range acoustic and optical components. Cut-off frequency of 1.5 THz is used^{36–38}. The amorphous-phase minimum lattice conductivity is also shown.

The calculated transport properties are illustrated in Figs. 11(a) to (c), namely S , σ_e , and $\kappa = \kappa_e + \kappa_L$ (κ_e is calculated with BoltzTraP), as a function of temperature, for three different hole concentrations n_p (the Fermi energy). The available experimental results³ are also shown. The Hall factor r_H and the Hall coefficient R_H , $n_p = r_H/eR_H$, are used in the calculations of n_p ^{9,19,20}, i.e.,

$$r_{H,\alpha} = \frac{\int_0^\infty \left(-\frac{\partial f_e^\circ}{\partial E_e}\right) \gamma_\alpha(E_e)^{3/2} dE_e \int_0^\infty \left(-\frac{\partial f_e^\circ}{\partial E_e}\right) \tau_e(E_e)^2 \gamma_\alpha(E_e)^{3/2} \left[\frac{d\gamma_\alpha(E_e)}{dE_e}\right]^{-2} dE_e}{\left\{ \int_0^\infty \left(-\frac{\partial f_e^\circ}{\partial E_e}\right) \tau_e(E_e) \gamma_\alpha(E_e)^{3/2} \left[\frac{d\gamma_\alpha(E_e)}{dE_e}\right]^{-1} dE_e \right\}^2}. \quad (21)$$

The trends in the temperature dependence of the TE properties are highly correlated with the thermal-disorder

behavior of PbTe. The Seebeck coefficient reaches a plateau after 500 K because the parabolic Σ -band is dominant above this temperature. The reduction in the electrical conductivity and the decrease in the total thermal conductivity also result from the thermal disorder and the effective mass changes. The heavy- and light-hole band convergence has a dominant role in the charge transport. As the band effective mass increases, the electronic contribution to the thermal conductivity is reduced⁴⁷. The D_e slope and its peaks near the band edge often dictate the overall performance, and semiconductors with heavy electron masses and multiple valleys have high ZT potential. For all predicted properties, there are good agreement with experiments³.

The lattice thermal conductivity tensor κ_L is determined using the equilibrium MD results and the Green-Kubo HCACF decay³⁶⁻³⁸. Figure 11(d) shows the predicted κ_L as a function of temperature, and demonstrates the suppression of the lattice thermal conductivity in the thermal-disordered structures (> 500 K). The MD results are: $\kappa_L(300$ K) = 3.1 and $\kappa_L(700$ K) = 0.9 W/m-K. The results show that κ_L decreases noticeably with increased temperature. The minimum conductivity κ_{\min} ^{48,49} for the amorphous phase is also shown, and gives $\kappa_{\min} \approx 0.32$ W/m-K (for $T > 2 T_D$, where $T_{D,\text{PbTe}} = 130$ K^{3,13}) using the PbTe properties³⁴. Figure 11(d) includes the results reported in³ using the total thermal conductivity and the Wiedemann-Franz law. The results of the Slack relation^{36,37} for the lattice thermal conductivity of crystal at high temperatures ($T > 0.1T_D$) are also shown in Fig. 11(d), using the properties listed in Table III. Prior to the onset of significant thermal disorder ($T < 500$ K), the MD results are in good agreement with the Slack relation ($1/T$ dependence). For $T > 500$ K, the thermal-disorder scattering becomes significant the lattice thermal conductivity becomes independent of temperature. This shows that the κ_L in thermal-disordered PbTe structure has two phonon transport regimes, pseudo-symmetry (single-band) and pseudo-amorphous (converged-band). The thermal-disordered structures represent a pseudo-amorphous phase which has high temperature anharmonic vibrations. In Fig. 11(d), we also decompose $\kappa_L(T)$ of PbTe into three components, namely, the acoustic short-range, acoustic long-range, and optical³⁶⁻³⁸, i.e.,

$$\kappa_L = \frac{1}{k_B V T^2} \left(A_{sh,A} \tau_{sh,A} + A_{lg,A} + \sum_i \frac{B_{i,O} \tau_{i,O}}{1 + \tau_{i,O}^2} \right) = \kappa_{L,sh,A} + \kappa_{L,lg,A} + \kappa_{L,O}, \quad (22)$$

where the τ_i is time constant, A_i and B_i are constants, and the subscripts sh , lg , A , and O refer to short-range, long-range, acoustic, and optical. From Fig. 11(d), the short- and long-range acoustic phonon contributions are dominant and most affected by the thermal disorder. The long-range acoustic contribution is almost saturated to the amorphous κ_L limit, but short-range is still changing up to 800 K. Note that κ_L decreases most noticeably in the converged-band regime.

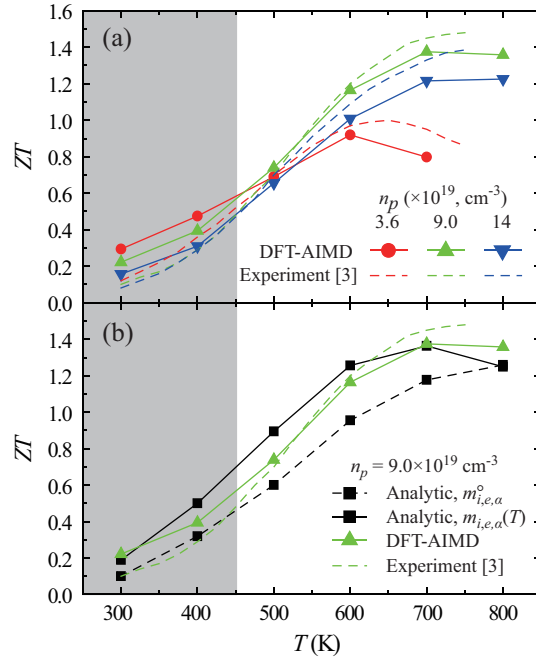


FIG. 12: (Color online) (a) Variations of the DFT-AIMD predicted ZT as a function of temperature for the p -type PbTe, at three different carrier concentrations n_p . The corresponding experimental results³ are also shown. (b) Variation of $ZT(T)$ obtained from the analytic model using constant $m_{i,e}^0$ and temperature-dependent $m_{i,e}(T)$, for the $9.0 \times 10^{19} \text{ cm}^{-3}$.

Combining all four TE properties from DFT and MD/Green-Kubo calculations, the predicted ZT of p -doped PbTe as a function of temperature, is shown in Fig. 12(a), along with the experimental results³. The results are for three different carrier concentrations n_p , including peak performance at $n_p = 9.0 \times 10^{19} \text{ cm}^{-3}$. The results for thermal-disordered structures are in good agreement with the experiments³. In order to confirm the thermal-disorder effective mass calculations, the results of two analytical models [constant $m_{i,e,\alpha}^{\circ}$ and temperature-dependent $m_{i,e,\alpha}(T)$] are shown in Fig. 12(b). With the temperature-dependent effective mass (Fig. 9), the analytical model prediction matches the DFT and the experimental results. In contrast, the constant effective mass [$m_{e,e,L}^{\circ} = m_{h,e,L}^{\circ} = 0.13$, $m_{h,e,\Sigma}^{\circ} = 1.3$] results¹⁸, i.e., neglecting the band convergence ($450 < T < 800 \text{ K}$) and divergence ($T < 450 \text{ K}$ and $T > 800 \text{ K}$), underestimate ZT over the entire temperature range. The thermal-disorder model and its effective mass of the altered band structures reveal the high- ZT PbTe behavior.

Due to the computation resource and time limitations, the time and length domains of AIMD simulations are limited. So, we have used the number of atoms in the periodic cell to simulate the extended system effects. In order to reliably predict the thermal-disordered structure and its electronic structures, by minimizing the statistical uncertainties, we use i) long enough simulation time to find well-converged structures, and ii) large number of atom in a simulation cell to minimize the drawbacks of the periodic boundary condition. These highly correlate with transport properties such as the phonon/electron lifetime and mean free path. Because of these limitations on the AIMD simulations, we pursued quantitative verifications such as the ones on the selection of representative snapshots, before entering the transport property calculations.

IV. CONCLUSION

In summary, we investigate the abnormal band convergence and TE properties of PbTe using *ab initio* thermal-disordered structures, i.e., at high temperatures the atoms do not occupy the ideal lattice positions, thus affecting the charge and phonon transports. Thermal disorder modifies the charge effective mass and suppresses the phonon short- and long-range acoustic contributions, resulting in high ZT for the converged-band, pseudo-amorphous structure (acoustic phonon suppression). Understanding of the thermal disorder provides an insight into design of improved TE chalcogenides.

ACKNOWLEDGMENT

This work is supported by the Center for Solar and Thermal Energy Conversion at University of Michigan, an Energy Frontier Research Center funded by the U.S. Department of Energy, Office of Science, Office of Basic Energy Sciences under Award Number DE-SC0000957. Fruitful discussions with Ctirad Uher are greatly appreciated.

-
- * Electronic address: kaviany@umich.edu
- ¹ Y. Noda, *Acta Cryst. B* **39**, 312 (1983).
 - ² G. A. Slack, in *CRC Handbook of Thermoelectrics*, edited by D. M. Rowe (CRC, Boca Raton, FL, 1995).
 - ³ Y. Pei *et al.*, *Energy Environ. Sci.* **4**, 2085 (2011).
 - ⁴ S. Ahmad, K. Hoang, and S. D. Mahanti, *Phys. Rev. Lett.* **96**, 056403 (2006).
 - ⁵ J. P. Heremans *et al.*, *Science* **321**, 554 (2008).
 - ⁶ K. Biswas *et al.*, *Nature Chem.* **3**, 160 (2011).
 - ⁷ J. Q. He *et al.*, *J. Am. Chem. Soc.* **133**, 8786 (2011).
 - ⁸ S. N. Girard *et al.*, *J. Am. Chem. Soc.* **133**, 16588 (2011).
 - ⁹ Y. Pei *et al.*, *Nature* **473**, 66 (2011).
 - ¹⁰ E. S. Božin *et al.*, *Science* **330**, 1660 (2010).
 - ¹¹ O. Delaire *et al.*, *Nature Mater.* **10**, 614 (2011).
 - ¹² Y. Zhang, X. Ke, P. R. C. Kent, J. Yang, and C. Chen, *Phys. Rev. Lett.* **107**, 175503 (2011).
 - ¹³ D. T. Morelli, V. Jovovic, and J. P. Heremans, *Phys. Rev. Lett.* **101**, 035901 (2008).
 - ¹⁴ C. Keffer, T. M. Hayes, and A. Bienenstock, *Phys. Rev. B* **2**, 1966 (1970).
 - ¹⁵ R. S. Alligaier, *J. Appl. Phys.* **32**, 2185 (1961).
 - ¹⁶ D. J. Singh, *Phys. Rev. B* **81**, 195217 (2010).
 - ¹⁷ L. M. Rogers, *Brit. J. Appl. Phys.* **18**, 1227 (1967).
 - ¹⁸ A. A. Andreev, *J. de Physique Colloque* **29**, C50 (1968).
 - ¹⁹ J. J. Harris and B. K. Ridley, *J. Phys. Chem. Solids* **33**, 1455 (1972).
 - ²⁰ C. J. Vineis *et al.*, *Phys. Rev. B* **77**, 235202 (2008).
 - ²¹ G. Kresse and J. Furthmüller, *Phys. Rev. B* **54**, 11169 (1996).
 - ²² P. E. Blöchl, *Phys. Rev. B* **50**, 17953 (1994).
 - ²³ Yu. I. Vesnin and Yu. V. Shubin, *Mater. Res. Bull.* **19**, 1355 (1984).
 - ²⁴ D. J. Singh and L. Nordstrom, *Planewaves, Pseudopotentials and the LAPW Method, 2nd Ed.* (Springer-Verlag, Berlin, Germany, 2006).
 - ²⁵ P. Blaha *et al.*, *WIEN2k, An Augmented Plane Wave + Local Orbitals Program for Calculating Crystal Properties* (K. Schwarz Technical University, Wien, Austria, 2001).
 - ²⁶ G. K. H. Madsen and D. J. Singh, *Comput. Phys. Commun.* **175**, 67 (2006).
 - ²⁷ E. Engel and S. H. Vosko, *Phys. Rev. B* **47**, 13164 (1993).
 - ²⁸ T. Chonan and S. Katayama, *J. Phys. Soc. Jpn.* **75**, 064601 (2006).
 - ²⁹ O. Qiu *et al.*, *Comput. Mater. Sci.* **53**, 278 (2011).
 - ³⁰ J. Gale and A. Rohl, *Mol. Simul.* **29**, 291 (2003).
 - ³¹ B. Houston, R. E. Strakna, and H. S. Belson, *J. Appl. Phys.* **39**, 3913 (1968).
 - ³² R. Dornhaus, G. Nimtz, and B. Schlicht, *Narrow Gap Semiconductors* (Springer-Verlag, Berlin, Germany, 1985).
 - ³³ E. A. Albanesi, C. M. I. Okoye, C. O. Rodriguez, E. L. Peltzer y Blanca, and A. G. Petukhov, *Phys. Rev. B* **61**, 16589 (2000).
 - ³⁴ H. Wang *et al.*, *Adv. Mater.* **23**, 1366 (2011).
 - ³⁵ Z. H. Dughaish, *Physica B* **322**, 205 (2002).
 - ³⁶ M. Kaviany, *Heat Transfer Physics* (Cambridge, New York, 2008).
 - ³⁷ B. L. Huang and M. Kaviany, *Phys. Rev. B* **77**, 125209 (2008).
 - ³⁸ H. Kim *et al.*, *Phys. Rev. Lett.* **105**, 265901 (2010).
 - ³⁹ D. I. Bilc, S. D. Mahanti, and M. G. Kanatzidis, *Phys. Rev. B* **74**, 125202 (2006).
 - ⁴⁰ A. Popescu, L. M. Woods, J. Martin, and G. S. Nolas, *Phys. Rev. B* **79**, 205302 (2009).
 - ⁴¹ S. Ahmad and S. D. Mahanti, *Phys. Rev. B* **81**, 165203 (2010).
 - ⁴² A. Shakouri *et al.*, *Microscale Thermophys. Eng.* **2**, 37 (1998).
 - ⁴³ G. S. Nolas, J. Sharp, and H. J. Goldsmid, *Thermoelectrics: Basic Principles and New Materials Developments* (Springer-Verlag, Berlin, Germany, 2001).
 - ⁴⁴ O. Delaire *et al.*, *Proceed. Nat. Acad. Sci.* **108**, 4725 (2011).
 - ⁴⁵ R. N. Tauber, A. A. Machonis, and I. B. Cadoff, *J. Appl. Phys.* **37**, 4855 (1966).
 - ⁴⁶ L. Xu, Y. Zheng, and J. C. Zheng, *Phys. Rev. B* **82**, 195102 (2010).
 - ⁴⁷ J. J. Pulikkotil, H. N. Alshareef, and U. Schwingenschlögl, *Chem. Phys. Lett.* **514**, 54 (2011).
 - ⁴⁸ D. G. Cahill, S. K. Watson, and R. O. Pohl, *Phys. Rev. B* **46**, 6131 (1992).
 - ⁴⁹ D. G. Cahill *et al.*, *Appl. Phys. Lett.* **96**, 121903 (2010).